Transient simulation of the last glacial inception. Part II: Sensitivity and feedback analysis

Reinhard Calov, Andrey Ganopolski, Vladimir Petoukhov, Martin Claussen, Victor Brovkin, Claudia Kubatzki

Potsdam Institute for Climate Impact Research, P.O. Box 601203, 14412 Potsdam, Germany

E-mail: calov@pik-potsdam.de

The sensitivity of the last glacial-inception (around 115 kyr BP, 115,000 years before present) to different feedback mechanisms has been analysed by using the Earth system model of intermediate complexity CLIMBER-2. CLIMBER-2 includes dynamic modules of the atmosphere, ocean, terrestrial biosphere and inland ice, the last of which was added recently by utilising the three-dimensonal polythermal ice-sheet model SICOPOLIS. We performed a set of transient experiments starting at the middle of the Eemiam interglacial and ran the model for 26,000 years with time-dependent orbital forcing and observed changes in atmospheric CO_2 concentration (CO_2 forcing). The role of vegetation and ocean feedback, CO_2 forcing, mineral dust, thermohaline circulation and orbital insolation are closely investigated. In our model, glacial inception, as a bifurcation in the climate system, appears in nearly all sensitivity runs including a run with constant atmospheric CO_2 concentration of 280 ppmv, a typical interglacial value, and simulations with prescribed present-day sea-surface temperatures or vegetation cover - although the rate of the ice-sheets growth is smaller than in the case of the fully interactive model. Only if we run the fully interactive model with constant present-day insolation and apply present-day CO_2 forcing does no glacial inception appear at all. This implies that, within our model, the orbital forcing alone is sufficient to trigger the interglacial-glacial transition, while vegetation, ocean and atmospheric CO_2 concentration only provide additional, although important, positive feedbacks. In addition, we found that possible reorganisations of the thermohaline circulation influence the distribution of inland ice.

1 Introduction

It is nowadays generally accepted that the reduction of boreal summer insolation drives the build-up of the ice masses. In the first part of this paper (Calov et al. 2004; hereafter cited as Calov et al. part 1), the capability of our model to simulate the last glacial inception with prescribed orbital and CO_2 forcing was demonstrated. Further, it was shown that the snow albedo feedback is the primary amplifier of the orbital forcing. Here, we analyse the role of other potentially important feedbacks and mechanisms related to terrestrial vegetation, atmospheric CO_2 concentration, mineral dust and changes in the thermohaline circulation.

Among several other sensitivity studies in their paper, Galleé et al. (1992) demonstrated the temperature-lowering effect of expanded tundra (at the expense of boreal forest) for LGM (last glacial maximum, 21 kyr BP) climate conditions with the zonally averaged LLN climate model. Later, Gallimore and Kutzbach (1996) compared time-slices at 115,000 kyr BP from the NCAR atmospheric GCM (general circulation model) CCM1 coupled to a mixed layer ocean. They showed that increased albedo representing expanded tundra area considerably lowers the Northern Hemisphere's temperature leading to a more persistent snow cover. DeNoblet et al. (1996) coupled interactively a biome (Prentice et al., 1992) global model with the LMD 5.3 GCM (fixed ocean), pinpointing with subsequent iterations of the biome model and the LMD-5.3 model the feedback mechanism through lowered temperature influencing the vegetation types and vice versa. Pollard and Thompson (1997) coupled the GENESIS2 atmospheric GCM, which includes mixed layer ocean and land surface, asynchronously to a vertically integrated ice-sheet model to simulate glacial inception with fixed 116 kyr orbital insolation and constant atmospheric CO_2 concentration. Despite these very favourable inception conditions, their North American inland-ice cover does not extend far enough to the south. A feedback analysis including vegetation using the Earth system model of intermediate complexity MoBidiC was carried out by Crucifix and Loutre (2002). But their model excludes the feedback through dynamic ice sheets.

In Khodri et al. (2001, 2003) it was shown, using the IPSL-CM2 atmospheric-ocean GCM, that an increased meridional atmospheric moisture transport and changes in

the ocean circulation might facilitate the growth of ice sheets. We add to their results with our investigation of a hypothesised southward shift of the convection sites in the North Atlantic and the implications of this for glacial inception, focusing especially on Scandinavia. The role of the thermohaline circulation of the North Atlantic has also been investigated by Wang and Mysak (2002) with another Earth system model of intermediate complexity.

The common picture of CO_2 reconstructions is of a more or less rapid drop of about 40 ppmv between 115 and 105 kyrs BP with a duration in the range from 5000 to 9000 years (Barnola et al. 1987; Petit et al. 1999; Fischer et al. 1999). Futhermore, the atmospheric CO_2 concentration in the palaeo-records starts to drop after the boreal summer insolation decreases. More than ten years ago, Verbitsky and Oglesby (1992) analysed the effect of a reduction in the atmospheric CO_2 concentration on the initiation of the ice sheets. They derived snowfall fields with the NCAR GCM1 by assuming an initial snow cover of 10 m for the Northern Hemisphere. This snowfall was used as input for a vertically integrated ice-sheet model, which then calculated the distribution of the ice sheets in the Northern Hemisphere. Verbitsky and Oglesby (1992) found in a simulation with a very low atmospheric CO_2 concentration of 100 ppmv a too low ice volume compared to the sea-level proxies. Although neither the change in orbital insolation nor the feedback of the ice sheets into the climate system are accounted for in their computations, they draw the conclusion that the atmospheric CO_2 concentration alone is not the “major player” in the initiation of glaciation during the Pleistocene. Vettoretti and Peltier (2004) investigated the importance of different orbital parameters and the CO_2 forcing with the CCCma AGCM2, which includes a mixed-layer ocean model. They concluded after a detailed analysis that for glacial inception the eccentricity-precession forcing has approximately the same magnitude as the CO_2 forcing. On the other hand, Vettoretti and Peltier concede that their model did not match the observed rate of sea-level drop during last glacial inception, because mechanisms such as vegetation feedback are still missing in their model.

The potential importance of mineral dust for the ablation of ice sheets during the last glacial cycle and, in particular, for the glacial termination have been discussed by Peltier and Marshall (1995). In their simulations with an ice-sheet model coupled to an

energy balance model they mimicked the increase of ablation through dust by increasing ablation artificially by a factor of three. In Calov et al. (part 1) it was shown with a physically based model for the dependence of snow albedo on dust (Warren and Wiscombe 1980) that during the latter stage of a glacial cycle, when the volume of the ice sheet is large enough, an increase of atmospheric dust could provide a negative feedback preventing further ice-sheet growth. Whether this is applicable to the initial stage of glaciation or only to the latter stages is not clear, however. Nonetheless, evidence has been found for an increased dustiness during glacial inception in the north-western Pacific (Porter 2001).

We start with a short summary of the model description (see Calov et al. part 1 for further details) and specification of the experimental setup (section 2). The role of mineral dust for glacial inception is discussed in section 3. Simulated climatic and glaciological fields in the course of glacial inception are discussed in section 4. A detailed inspection and analysis of the role of terrestrial vegetation and the ocean follow in section 5. In addition, the role of atmospheric CO_2 concentration and orbital insolation will be studied in section 6. The implications of possible changes of the thermohaline circulation in the Atlantic during last glacial inception are examined closely in section 7. We close with a discussion of our findings (section 8) and a summary of our results together with concluding remarks (section 9).

2 The model and the experimental setup

2.1 The model

The Earth system model of intermediate complexity CLIMBER-2 (Petoukhov et al. 2000) encompasses the atmosphere, ocean, terrestrial biosphere and ice sheets. The latter have been recently integrated into the model by inclusion of the polythermal ice-sheet model SICOPOLIS (Greve 1997a; 1997b) and a newly developed bi-directional coupling module named SEMI (Surface Energy and Mass balance Interface). A detailed description of the models and the coupling is provided in Calov et al. (part 1).

CLIMBER-2 is based on a statistical-dynamical atmosphere model with a low spatial resolution (7 longitudinal sectors and 18 latitudinal belts), and the zonally averaged ocean module accounts for three separate ocean basins, the Atlantic, Indian and Pacific. Atmosphere and ocean interact through the surface fluxes of heat, fresh water and momentum.

SICOPOLIS simulates the time-dependent extent, thickness, velocity, temperature, water content and age for grounded ice sheets. Furthermore, possible basal layers of temperate ice are detected by fulfilling the Stefan-type conditions at the transition surface between cold and temperate ice. The bedrock responds to the load of the ice through the buoyancy forces of the asthenosphere.

The coupling module (SEMI) calculates the energy and mass balance on the fine grid of SICOPOLIS - the Northern Hemisphere is resolved by a grid spacing of 1.5° for the longitude and 0.75° for the latitude - using interpolated atmospheric characteristics (air temperature and humidity, long-wave and short-wave radiation, precipitation) from the CLIMBER-2 model and accounting for the orography on the fine grid. In turn, SICOPOLIS provides CLIMBER-2 with the temporal change of orography and fractions of land and glaciers.

2.2 The experimental setup

The model is run synchronously over 26,000 years starting at 126 kyr BP and ending at 100 kyr BP, spanning about one precession cycle. The global and seasonal change of orbital insolation is computed with the algorithm after Berger (1978), and in all experiments except one (experiment AOVID_280), the atmospheric CO_2 concentration is prescribed after Barnola et al. (1987). Because the extent of the Greenland ice sheet during the Eemian is not known precisely, we use its present-day equilibrium distribution as initial condition. The complete setting is explained in Calov et al. (part 1). In experiment AOVI (see Table 1 for the description of the experimental acronyms), the dust-deposition rate was held constant at modern values according to Mahowald et al. (1999). Experiment AOVI was performed with synchronous and fully interactive coupling between atmosphere, ocean, vegetation and ice-sheet components of the model.

In the other experiments the dust-deposition rate is coupled to the inland-ice volume through the linear parameterisation

$$D(\lambda,\varphi,t) = (1-w(t))D_{PD}(\lambda,\varphi) + w(t)D_{LGM}(\lambda,\varphi), \qquad (1)$$

where t is the model time. D_{PD} and D_{LGM} are the present-day dust-deposition rate and the LGM dust-deposition rate, respectively. The weights in Eq. 1 are determined through $w(t) = V(t)/V_{LGM}$. We compute the evolution of the inland-ice volume of the Northern Hemisphere V with the ice-sheet model SICOPOLIS. $V_{LGM} = 48$ million km^3 is an empirical estimate of the LGM Northern Hemisphere's inland-ice volume corresponding roughly to 110 m sea level drop (approximately the LGM volume of the Northern Hemisphere ice sheets excluding Greenland). The dust-deposition rates D_{PD} and D_{LGM}, interpolated to the grid of the ice-sheet model, are taken from Mahowald et al. (1999). Mahowald et al. (1999) computed the dust-deposition rates with an entrainment and transport model employing wind and precipitation fields of a GCM and applying dust sources which are modelled with the BIOME3 terrestrial biosphere model. Eq. 1 is a heuristic approach to parameterise the approximate time dependence of the dust-deposition rate during last glacial inception. We argue as follows. With increased ice volume the sea level drops and the continental shelf regions are exposed to the air. These regions can serve as additional dust sources. Therefore, it appears to be reasonable to use the ice volume as a parameter. It is natural to assume a linear dependence as a first approach.

The experiments where the ice volume is dependent on dust-deposition rate are denoted by inclusion of the letter "D", e.g. experiment AOVID. Further experiments were with fixed present-day vegetation cover (AOID) or with "fixed ocean" (seasonal variations of sea-surface temperature and sea-ice cover were held on their present-day values, AVID) or with fixed atmospheric CO_2 concentration at present-day level (experiment AOVID_280). Additionally, we introduced an artificial fresh-water perturbation to the Atlantic thermohaline circulation, which leads to a southward shift of the North Atlantic convection site (experiment AOVID_THC).

AOVI	Atmosphere, Ocean, Vegetation and Ice sheets.
AOVID	Atmosphere, Ocean, Vegetation, Ice sheets and Dust.
AOID	Atmosphere, Ocean, Ice sheets and Dust. Vegetation fixed.
AVID	Atmosphere, Vegetation, Ice sheets and Dust. Ocean fixed.
AID	Atmosphere, Ice sheets and Dust. Ocean and vegetation fixed
AOVID_280	Atmosphere, Ocean, Vegetation, Ice sheets and Dust. CO_2 fixed.
AOVID_THC	Atmosphere, Ocean, Vegetation, Ice sheets and Dust. Thermohaline circulation changed by a fresh-water perturbation in the Nordic Seas.
AOVID_PDI	Atmosphere, Ocean, Vegetation, Ice sheets and Dust. Isolation fixed.
CTRL	Steady-state run with constant pre-industrial conditions

Table 1: Notation of the experiments. Here, 'fixed' means that present-day conditions are used for the module or the quantity. For the experiment with fixed atmospheric CO_2 concentration the pre-industrial value of 280 ppmv applies. All experiments are transient simulations except for experiment CTRL.

3 The role of mineral dust

In this section we assess the potential role of the dust impact on snow albedo for the Northern Hemisphere's glaciation by comparison of experiments AOVID and AOVI. The physical basis of the dependence of the albedo of snow on mineral dust had been pointed out in Calov et al. (part 1).

Before we present results of experiments AOVID and AOVI we briefly discuss the distribution of the dust fields after Mahowald et al. (1999) in those regions in the Northern Hemisphere which are important for our results. Mahowald's present-day dust-deposition rate (Fig. 1a) has a pronounced maximum in the centre of the Eurasian continent (about $10\ g\ m^{-2}\ yr^{-1}$ near the Caspian Sea) decreasing to the north, east and west, and is relatively low in eastern Siberia, Scandinavia, Greenland and over the Arctic Ocean. For the North American continent, the present-day dust-deposition rate overall is low except for the Canadian Archipelago. At LGM, Mahowald et al. (1999) obtained a 20 times higher dust-deposition rate in high latitudes; see Fig. 1b for the ratio of LGM to present-day dust-deposition rate. While the increase of the dust-deposition rate at LGM compared to present day is relatively low in Scandinavia and the central part of North America (1 to 5-fold), it is high in central and eastern Eurasia (10 to 200-fold) as well as in southern Alaska (50 to 100-fold), and very high in northern Alaska (more than 200-fold).

Fig. 2 compares time series of global sea level from proxy data for 125 to 100 kyr BP with computed sea-level changes in experiments AOVI and AOVID. While nearly all proxy sea-level data between 125 and 110 kyr BP have similar characteristics – a high level before 115 kyr BP and a rapid drop down to about –50 m thereafter - the sea level from corals (Bard et al. 1990; Chappell et al. 1996; Eisenhauer et al. 1996, Cutler et al. 2003; Gallup et al. 2002; Zhu et al. 1993) and from benthic $\delta^{18}O$ after Waelbroeck et al. (2003) is up to 20 m higher between 110 and 100 kyr BP than the old SPECMAP curve (Imbrie et al. 1984). While the observed low stand of sea level at about 110 kyr BP is displayed very well in experiment AOVID, the drop is overestimated in experiment AOVI. While, finally, the sea level in experiment AOVID rises after 110 kyr BP, in experiment AOVI it monotonically decreases between 118 and 100 kyr BP.

Fig. 3 shows the extent of inland ice on the Northern Hemisphere in experiments AOVID and AOVI at 115 kyr BP, a time of low boreal summer insolation, at 110 kyr BP, when the reconstructed ice volume is high, and at 105 kyr BP, a time of high boreal summer insolation. While the ice extent in North America is similar at all three time slices depicted here, the inland-ice cover is drastically different in Eurasia. At 115 kyr BP, the southern ice margin of the Laurentide ice sheet reaches approximately 50° N in

both simulations. In experiment AOVI, it extends slightly farther to the south than in experiment AOVID (Fig. 3a,b). In experiment AOVID, northern Alaska and a small part of the Hudson Bay are free of inland ice, but they are covered by inland ice in experiment AOVI. According to Hamilton (1994), only parts of southern Alaska were ice covered, which correspond to the ice extent seen in experiment AOVID. The Fennoscandian inland ice in experiment AOVI reaches farther southwest than that in experiment AOVID. An isolated glaciation on and eastward of the New Siberian Islands is seen in experiment AOVID. In north-eastern Eurasia - eastwards of about 100° E -, experiment AOVI simulates a widespread glaciation, while experiment AOVID shows only a minor glaciation there. While the inland-ice cover in Eurasia in experiment AOVID increases from 115 to 110 kyr BP (Fig. 3c) and decreases from 110 to 105 kyr BP (Fig. 3e), it increases between all considered time slices in experiment AOVI (Fig. 3b,d,f). Between 110 and 105 kyr BP, the Fennoscandian inland ice in experiment AOVID is retreating. This agrees with geological findings by Kleman et al. (1997) and Mangerud (1991). A closer discussion of the Fennoscandian inland ice will follow in section 7. Overall, experiment AOVID gives a more realistic inland-ice cover of the Northern Hemisphere during the glacial-inception episode.

A large part of the differences between results obtained in experiments AOVID and AOVI can be explained by the direct impact of the dust distribution on the albedo of snow; with a higher dust-deposition rate the albedo of snow is reduced, and the snowmelt is amplified - recall that the dust-deposition rate in experiment AOVID is the weighted mean (eq. 1) between the present-day and the LGM values. Regions like north-eastern Eurasia and northern Alaska, where the dust-deposition rate during LGM is high, show little or even no glaciation in experiment AOVID. Regions with a moderate LGM dust-deposition rate mostly show a comparable inland-ice cover in experiments AOVID and AOVI (see the Laurentide, the Cordilleran and the Fennoscandian ice sheets in Fig. 3). The glaciation in north-eastern Eurasia is highly sensitive to dust in our simulation, because snowfall is low there. The low snowfall enhances the sensitivity of the ice sheets to mineral dust, because the dust concentration in snow for a given dust-deposition rate is inversely proportional to the snowfall. In addition, the snow albedo is a function of the dust concentration in the snow. Therefore, changes in the dust-deposition rate have the

strongest impact on the surface albedo in areas with low snowfall. In experiment AOVI, where the dust-deposition rate is held fixed to its modern value, the snow-albedo feedback (Calov et al. part 1) causes under reduced boreal summer insolation a rapid expansion of inland-ice cover in north-eastern Eurasia, similar to that in northern North America (see Fig. 3f). The big ice sheet in north-eastern Eurasia is the reason why the sea level curve of experiment AOVI has little tendency to level off (Fig. 2). In experiment AOVID, there is only minor glaciation in north-eastern Eurasia, because the glacial dust-deposition rate there is much higher than the modern one, which leads to stronger melting in the ablation zone of the ice sheet as compared to experiment AOVI. This hampers the snow-albedo feedback. Because experiment AOVID produces more realistic results than experiment AOVI, we decided to apply time-dependent dust for all further simulations in this paper.

4 Glacial inception and climate changes

In our simulation, the glaciation of North America starts in Baffin Island and northern Quebec at 118 kyr BP (Fig. 4a). Small ice nuclei are seen over the Canadian Archipelago and in the southern part of Alaska. After only 1 kyr vast areas of northern North America (the Canadian Archipelago, the Keewatin region, the northern part of Cordilleran and parts of Alaska) are covered with relatively thin ice (Fig. 4b). Interestingly, an “instantaneous glaciation” in parts of North America was discussed by Ives et al. (1975) pointing to different glaciation processes in Fennoscandia (slow) and in northern North America (fast). At 110 kyr BP, the southern ice margin of the North American inland ice reaches approximately 56° N (Fig. 4c). In particular, the Hudson Bay lowlands and James Bay lowlands are ice covered at that time. Our evolution of inland-ice cover is broadly similar to those based upon reconstructions of glaciation from geological evidence reviewed by Clark et al. (1993): they reported that the glacial inception first developed during early MIS 5 (MIS, Marine Isotope Stage, see the top of Fig. 2) in Keewatin, Quebec and Baffin Island. Our simulation is in good agreement with interpretations of drift lineations by Boulton and Clark (1990). Such lineations enable (relative) dating of ice-flow directions. Our modelled direction of motion of inland ice and its time frame

depicted in Figs. 4a to 4c corresponds fairly well with two flow sets of such drift lineations; see “set A” and “set B” in Fig 10 by Boulton and Clark (1990). They interpret flow set A, which is located NE of Keewatin, as indicative of an “ice sheet expansion from centres of initiation in N Baffin Island or NE Keewatin”. Further, Boulton and Clark attribute flow set B to a “major expansion of ice into Manitoba and Saskatchewan”. It is important to note that Bolton and Clark allocate flow set A and flow set B to the time of the last glacial inception.

The evolution of inland ice (Fig. 5) shows more ice in North America than in Europe for all scenarios. (Note that the inland ice in Scandinavia, Svalbard and Iceland are shown, while the contributions of Greenland and north-eastern Eurasia are not displayed in Fig. 5.) The North American ice volume and area (Fig. 5a,b) both increase faster than European ice volume and area (Fig. 5c,d). While ice volume and ice area change in a sudden transition from a slow to a fast increase in northern North America, both quantities vary much more gradually in northern Europe. This bifurcation transition (Calov et al part 1) is more pronounced for ice area than for volume, pointing out that the glacial inception in North America started with a rapid development of large area of thin ice followed by a slower increase of ice volume. In experiment AOVID, the North American inland-ice cover reaches the interglacial-glacial bifurcation, here seen as a transition from slow to fast increase of the ice area, at 117.4 kyr BP. Within 300 years the ice area increases by about 4 million km^2, which is approximately 40% of the maximum ice area of this experiment. At the end of all scenarios (100 kyr BP), most of the ice is still present in North America, while it completely vanishes or strongly decreases in Europe at that time. The inland ice in North America remains, because local cooling is sustained by the presence of expanded inland-ice cover.

Our model simulates the onset of glaciation at the same time as the Earth system model of intermediate complexity of Wang and Mysak (2002). The total ice volume in one of their simulations, named run 1 in their paper, is about a factor of 2/3 smaller than in our experiment AOVID. This (moderate) difference could partly be due to the missing of vegetation feedback in their model. However, there are larger differences in the distribution of continental ice cover between the model of Wang and Mysak (2002) and our model. While in the model of Wang and Mysak (2002) the ice volume at 110 kyr BP

is distributed half-and-half in North America and Eurasia, our model simulates much more inland ice in North America than in Eurasia then; at 110 kyr BP, experiment AOVID simulates about 4 times more ice volume in North American than in Eurasia. This is partly explainable with the inclusion of dust in our simulation.

Fig. 6 shows temperature and precipitation anomalies, with present-day values as reference, in boreal summer (average for June, July and August, JJA) on the coarse grid of CLIMBER-2 at 118 and 115 kyr BP in experiment AOVID. At 118 kyr BP, the simulated summer temperature over North America and northern Eurasia is 3°C lower than at present day (Fig. 6a), which is mainly due to changes in orbital forcing. Insolation during summer (JJA average) at 118 kyr BP at 65°N was about 10 $\mathrm{W\,m^{-2}}$ lower than during present-day summer. At that time, the atmospheric CO_2 concentration was approximately the pre-industrial present-day value. Indeed, the corresponding plot for the anomaly between AOVID_280 and CTLR (the anomaly in a run with constant pre-industrial present-day CO_2 concentration, not shown here) looks very similar in structure and absolute values. These results corroborate our conclusion that in the Northern Hemisphere, Fig. 6a mainly depicts the response of temperature to the summer insolation. Positive feedback mechanisms, like the southward retreat of boreal forest, contribute to this temperature decrease also. At 118 kyr BP, the simulated inland-ice cover is small. In the Southern Hemisphere, the temperature drop at 118 kyr BP is about 0.5°C, which is a combined response to the interhemispheric ocean-heat transport and a slight reduction of atmospheric CO_2 concentration.

The summer precipitation at 118 kyr BP (Fig. 6b) decreases in most parts of the Earth. A reduction of the Asian summer monsoon by 1.0 mm $\mathrm{day^{-1}}$ can clearly be seen. Interestingly enough, An (2000) reports that such a weakening is qualitatively seen - at least for the present-day to LGM contrast - in the proxy data. A southward shift of the Intertropical Convergence Zone can be detected by the two bands of positive and negative precipitation anomalies.

At 115 kyr BP, the anomalies of boreal summer temperature (Fig. 6c) have increased by a combination of processes: the boreal summer insolation decreases substantially at 115 kyr BP and the atmospheric CO_2 concentration has become lower by about 40 ppmv. Over northern North America, the summer temperature drops by 12°C, a

decrease that can be partly attributed to local cooling due to the surface elevation and albedo of the Laurentide ice sheet. Over north-eastern Asia, the temperature decreases by 6°C. The temperature drop of 2°C on the southern Hemisphere cannot be explained by either the limited glaciation there, or by the negligible decrease of summer (JJA) insolation (about 0.3 $\mathrm{W\,m^{-2}}$ at 65°S). In our model, the drop of temperature over the Southern Hemisphere is caused by lowered atmospheric CO_2 concentration and by the intensification of interhemispheric exchange of heat via the ocean circulation.

At 115 kyr BP, the precipitation anomalies (Fig. 6d) over Canada double in comparison with that at 118 kyr BP (0.4 mm $\mathrm{day^{-1}}$). The Asian summer monsoon further weakens.

5 The role of vegetation and ocean feedbacks

In this section, we investigate the impact of dynamic vegetation and ocean (sea-surface temperature and sea-ice cover) by comparing results with the correspondent modules switched on with those obtained by keeping them fixed at present-day conditions. The evolution of total ice area - except for the Greenland ice area which is excluded in this figure - for different model configurations with and without interactive ocean and/or vegetation is depicted in Fig. 7a. In the simulation with “fixed” vegetation we applied the simulated present-day vegetation distribution as shown in Fig. 8a. It is seen from Fig. 7a that experiments AID (atmosphere, ice sheets and dust switched on, see also Table 1) and AVID (with vegetation additionally switched on) both show a similar, but weak increase of ice area. These two runs alone suggest that the impact of the vegetation feedback (southward retreat of boreal forest, see Fig. 8) on the build-up of inland ice is weaker than the impact of the ocean (sea-surface temperature and sea-ice extent). However, the experiments with a dynamic ocean (i.e., AOID, AOVID) differ strongly from each other with respect to the change in inland-ice cover. At 110 kyr BP, the ice area in experiment AOVID is nearly a factor 2 larger than the inland-ice cover in experiment AOID. Obviously, the vegetation and the ocean feedbacks are amplifying each other. Such a synergy effect is described in Ganopolski et al. (1998), Braconnot et al. (1999) and Claussen (2001). Finally, it is clearly seen that the timing of the interglacial-glacial

bifurcation (Calov et al., part 1) depends on the model configuration; e.g., in experiment AOVID, which includes interactive vegetation and ocean, this bifurcation appears some 1000 years earlier than in experiment AID, in which vegetation and ocean are fixed to present-day conditions.

Fig. 9 illustrates the impact of the vegetation feedback (and the synergism associated with it) on climate change. At 125 kyr BP, the difference of the annual temperature between experiments AOVID and AOID is up to 1.2 °C in Canada and 1 °C in north-eastern Eurasia. This positive temperature anomaly is mainly due to the northward advance of boreal forest (compare Fig. 8a with 8b) for the warmer Eemian climate in experiment AOVID relative to experiment AOID – recall that in experiment AOID the present-day pre-industrial vegetation is prescribed throughout the whole simulation. The vegetation feedback amplifies the Eemian warming. Conversely, the cooling trend triggered by the decreasing boreal summer insolation is facilitated by the vegetation feedback too: just before the interglacial-glacial bifurcation at 118 kyr BP, when there is only minor inland-ice cover in our model, the anomaly between experiments AOVID and AOID becomes negative. The temperature anomaly in the centre of North America and in north-eastern Eurasia now amounts to -0.6°C (Fig. 9b). While the time slices at 125 and 118 kyr BP displayed feedbacks mainly through interplay of vegetation and sea ice feedbacks (Ganopolski et al. 1998; Brovkin et al. 2003), there is an additional feedback through the inland ice, when the climate-cryosphere system is in glacial state. At 115 kyr BP, the temperature differences between experiments AOVID and AOID reach up to -3°C (Fig. 9c). We emphasise that in an analogous experiment without dynamic inland ice, the anomalies at 118 and 115 kyr BP are very similar (not illustrated here). This shows that the ice-sheet dynamics brings an additional synergy into the climate system. Therefore, a more detailed feedback analysis with additional runs is warranted, which will be presented in a forthcoming paper.

6 The role of atmospheric CO_2 concentration and orbital insolation

As shown by Loutre and Berger (2000), we have confirmed that the changes of atmospheric CO_2 concentration during the last glacial inception alone are not sufficient to take the system into glacial state. In experiment AOVID_PDI (PDI stands for present-day insolation), the orbital insolation is held at its present-day value throughout the whole simulation. The magnitude of the present-day boreal summer insolation lies approximately between that at 125 kyr BP (Eemian optimum) and at 115 kyr BP. In experiment AOVID_PDI, the inland-ice area in North America and Eurasia remains negligibly small; the drop in the prescribed atmospheric CO_2 concentration of nearly 40 ppmv does not push the system into the glacial state (Fig. 7b). Nonetheless, the change of atmospheric CO_2 concentration has to be accounted for, which follows from comparison of experiments AOVID and AOVID_280 (Fig. 7b). In the former experiment, the atmospheric CO_2 concentration after Barnola et al. (1987) is prescribed, while in the latter one, it is held constant at its pre-industrial value of 280 ppmv through the whole simulation. Of course, in experiments AOVID and AOVID_280 (and all others except AOVID_PDI) the change of orbital insolation according to Berger (1978) is used. In experiment AOVID_280, the climate system runs into glacial state, but the inland-ice cover is smaller than in experiment AOVID. At 110 kyr BP, experiment AOVID simulates about a factor of 1.5 more ice area than experiment AOVID_280.

Experiments AOID and AOVID_280 both simulate lower ice volume and area (Fig. 5c,d) than experiment AOVID does, which illustrates the impacts of variable atmospheric CO_2 concentration and interactive vegetation (see Fig. 8). By comparing experiment AOID with experiment AOVID_280 it can be seen that the inland-ice cover reacts in North America in a different way than in northern Europe. Between about 118 and 105 kyr BP, experiment AOID simulates less ice volume than experiment AOVID_280 in North America, while the ice volume in northern Europe is larger or (approximately) equal in the same runs during the same time span. This is because vast areas of North America are soon covered with ice, which replaces the vegetation there, while in northern Europe (and Eurasia) the area where vegetation in the course of expanding inland-ice cover may evolve, remains much larger. Between 118 and 113 kyr the large drop of the atmospheric CO_2 concentration (experiment AOID) and the retreat of boreal forest (experiment AOVID_280) lead to the same inland-ice cover in northern

Europe. In North America there is an additional feedback through the strong increase of inland-ice cover. After about 113 kyr BP, the forest fraction in experiment AOVID_280 increases, thereby leading to warming in northern Europe and less ice volume there than in experiment AOID. Fig. 5b shows that the glacial inception in experiment AOVID_280 appears slightly later than that in experiment AOVID, which is attributed to the drop of the atmospheric CO_2 concentration and subsequent greenhouse cooling. Experiment AOID has a slightly later glacial inception than either AOVID or AOVID_280, because the vegetation feedback is neglected here.

7 The possible influence of the thermohaline ocean circulation

It was proposed in several studies (Tarasov and Peltier 1997, Khodri et al, 2001; Khodri et al, 2002) that reorganisation of Atlantic thermohaline circulation via a reduction of northward heat transport might serve as an additional positive feedback facilitating glacial inception. In particular, Khodri et al. (2001), using a coupled climate model, have found that the orbital configuration corresponding to 115 kyr BP leads to a reduction of the thermohaline circulation and less intensive convection in the Nordic Seas as compared to the present climate state. However, because the model used in the study of Khodri et al. (2001; 2002) did not include ice-sheet dynamics, it was not possible to quantify whether these changes in the ocean circulation could substantially contribute to the build up of the ice sheets in the Northern Hemisphere. To address this issue, we performed the sensitivity experiment AOVID_THC in which we imposed a considerably larger change in the ocean circulation than that simulated in Khodri et al (2001).

As it was shown in previous studies (e.g. Ganopolski and Rahmstorf, 2001), CLIMBER-2 reveals two stable modes of operation under full glacial conditions (similar to LGM): a “cold” (stadial) mode and a “warm” (interstadial) mode. These two modes of operation are characterised by different locations of North Atlantic Deep Water (NADW) formation – in the cold mode, NADW is formed about 15^o farther south than in the warm mode. In our experiments, both volume and area of ice sheets remain considerably smaller than at LGM. Therefore, a transition between warm and cold modes did not occur naturally during transient simulations. To mimic such transitions, we imposed the change

of one of the model parameter – the so-called "freshwater bypass parameter" (see Ganopolski and Rahmstorf, 2001) at 115.5 kyr BP. A change in this parameter leads to an increased fresh-water flux to the Nordic Seas, which causes a rapid transition from the warm to the cold mode of the thermohaline circulation, a weakening of NADW formation and considerable cooling over the North Atlantic.

The anomalies between experiments AOVID and AOVID_THC at 110 kyr in Fig. 10 reveal the influence of a shift of the convection site of the conveyor belt in the North Atlantic on the climate. The minimum in the precipitation anomaly of about -0.7 mm yr^{-1} is located over northwest Europe (Fig. 10a). The precipitation anomaly is with -0.4 to -0.3 mm yr^{-1} over eastern Canada less pronounced than that over northwest Europe. The minimum in the summer temperature anomaly of about -4.2° is centred over the North Atlantic (Fig. 10b). Contrary to the precipitation anomaly, the summer temperature anomaly is equally strong over northwest Europe and eastern Canada. Our model reproduces the interhemispheric sea-saw effect (Crowley 1992); there is warming on the Southern Hemisphere and cooling on the Northern Hemisphere, because less heat is pumped from the south to the north in AOVID_THC. The change of temperature and precipitation pattern induced by the switch of the ocean thermohaline circulation from warm to cold mode has interesting consequences for the ice cover in Fennoscandia (Fig. 11). While for an ocean in warm mode there is a thick ice sheet with one ice dome, the ice sheet modelled with an ocean in cold mode has two slightly lower domes. Furthermore, the cold-mode Fennoscandia inland ice is shifted several hundred kilometres to west-southwest. This is caused by reduced summer precipitation (Fig. 10a) and lower temperatures (Fig. 10b) for a cold-mode ocean. The temperature decrease is consistent with a reduced summer melting of ice, which causes the west-southwest advance of the Fennoscandian ice margins. The change in precipitation reduces the mass balance, which cannot be compensated by the colder temperature in the north of Scandinavia in experiment AOVID_THC.

In conclusion, the effect of a change in the Atlantic thermohaline circulation on the Northern Hemisphere's inland-ice cover is quite complex. While the temperature drop through a southward shift of convection site influences both Europe and North America, the precipitation drop over Europe is stronger than over northern North America (Fig.

10). This happens because the western Pacific and the mid-latitude Atlantic are the moisture sources for North America and the northern North Atlantic is the main moisture source for Scandinavia (see e.g. Peixoto and Oort 1992). Therefore, there is more inland ice (Fig. 5) in North America for a cold-mode ocean than for a warm-mode ocean. The existence of a large ice sheet in North America additionally cools (and dries) the whole climate system, in particular the Scandinavian region - an effect which additionally contributes to the thinning and southwestward shift of the Fennoscandian ice sheet. Interestingly, our experiment AOVID_THC with two ice domes at 110 kyr BP agrees better with a reconstruction after Kleman et al. (1997) than experiment AOVID.

In contrast to what happens over Scandinavia, ice volume and ice area in North America both show a greater increase in experiment AOVID_THC than in experiment AOVID (Fig. 5a, b), which is consistent with the differences in temperature and precipitation between AOVID_THC and AOVID (Fig. 10a, b); in northern North America the precipitation drop is smaller than in Scandinavia, while the temperature decreases in both regions are comparable. Thus, our results suggest that changes in the Atlantic thermohaline circulation might affect the rate of growth of the ice sheets, but it is unlikely to be a major positive feedback.

8 Discussion

We have presented transient simulations of the last glacial inception. Experiment AOVI, which uses the present-day dust-deposition rate, displays the main features of the last glacial inception, i.e., a rapid expansion of inland ice on the Northern Hemisphere at about 115 kyr BP. However, experiment AOVI yields a somewhat larger inland-ice cover in northeastern Eurasia and Alaska than what is indicated by geological evidence. Such an overestimation of inland-ice cover in eastern Eurasia had already been noticed by others (e.g. Marsiat 1994; Calov and Marsiat 1998). In experiment AOVID, where the dust deposition rate was allowed to vary between modern and LGM values, both sea-level change and geographical extent of ice sheets are in much better agreement with palaeodata. It might be possible that our parameterisation (equation 1) overestimates the

dust-deposition rate during the last glacial inception. However, the data sources for dust do not give a homogenous picture – the dust time series rather depend on the location where the data was taken. In particular, Porter (2001) reports an increased mineral dust concentration in the Northwestern Pacific during glacial inception, which supports our approach. Our model does not account for the radiative effect of dust (Claquin et al. 2003). The impact of the radiative effect of mineral dust on the interglacial-glacial climate change will be investigated in a forthcoming study. Here, we demonstrated the importance of one aspect of mineral dust for ice sheets in the climate system, namely its relevance for ablation of snow and ice.

It is noteworthy that our simulated ice volume agrees well with SPECMAP data for MIS 5e to 5c (Fig. 2). Coral data indicate less ice volume at MIS 5c than the SPECMAP reconstruction (Fig. 2). Since it is known that $\delta^{18}O$ data represent a mixed signal of sea level and deep-ocean temperature changes, it is probable that the sea level rise during MIS 5c was considerably larger in reality than displayed by the $\delta^{18}O$ signal. If this is the case, then our model underestimates the decrease of ice volume after glacial inception. In this respect, it is interesting to note that in experiments with the LLN climate model, the ice volume returns to the interglacial level during MIS 5c. The reasons for such a differing sensitivity of climate-ice sheet models to the orbital forcing are still unknown.

In our model, glacial inception is triggered by a decrease in boreal summer insolation. Once a critical threshold is crossed, the snow-albedo feedback pushes the system from a interglacial to a glacial state (Calov et al. part 1). Other mechanisms in the climate system such as feedbacks through atmospheric CO_2 concentration, vegetation and ocean amplify the strength of the interglacial-glacial transition. Our results suggest the existence of strong synergy in the climate system regarding vegetation and ocean feedbacks during glacial inception.

Vegetation has been recognised as one of the important components of the climate system (by, e.g., Claussen 2004). Our vegetation model (VECODE as a part of CLIMBER-2) displays a broad picture of the dynamics of vegetation. At the Eemian interglacial, CLIMBER-2 shows an increase of forest cover in the northern high latitudes while during the last glacial inception, a retreat of boreal forest is simulated. Our model

shows that the dynamics of vegetation together with the ocean feedback amplifies glacial inception. This corroborates earlier results by deNoblet et al. (1996). In their simulations, which were done without inland-ice dynamics, the vegetation feedback helped to create favourable conditions for the growth of the mid-latitude inland ice. Crucifix and Loutre (2002) showed that in their model, MoBiDiC, interactive vegetation cover is crucial to yield a perennial snow cover north of 60°N after approximately 122 kyr BP. Indeed, MoBiDiC has about two times higher sensitivity to changes of forest cover in the latitudinal zone between 60° and 70°N than CLIMBER-2 (Brovkin et al., 2003). Recently, Kageyama et al. (2004) presented a study of last glacial inception with CLIMBER-2 coupled to the ice-sheet model GREMLINS. The sensitivity to interactive vegetation in their coupled model appears to be higher than that in our model. This is because Kageyama et al. (2004) kept the vegetation fixed at the rather warm condition at 126 kyr BP in their atmosphere-ocean-ice-sheets simulation and not at present-day condition as in our corresponding experiment AOVI. Meissner et al. (2003) presented results from simulations with the UVic Earth System model using a constant orbital forcing (representative for 116 kyr BP) and a constant atmospheric CO_2 concentration of 240 ppmv. Meissner et al. (2003) confirm the significance of vegetation feedbacks. In their model, synergies and feedbacks related to vegetation dynamics appear to double atmospheric cooling during the last glacial inception. Interestingly enough, Meissner et al. (2003) find that without feedbacks related to vegetation dynamics, monthly averaged September snow, which the authors refer to as perennial snow, still occurs in their model over Baffin Island. This suggests the possibility of glacial inception without any vegetation feedback as seen in the study presented here.

Whether or not changes in the Atlantic circulation took place at the last glacial inception, as simulated in experiment AOVID_THC, cannot yet be answered. Wang and Mysak (2002) found an intensified thermohaline circulation during last glacial inception in their Earth system model of intermediate complexity. Such an intensification of the thermohaline circulation is similarly reproduced in our experiment AOVID too; but this is not shown explicitly in our paper. In experiment AOVID_THC, we investigate the impact of an induced *decrease* of the thermohaline circulation, which is even stronger than that reported by Khodri (2001). Kageyama et al. (1999) simulated an increase in

precipitation over the North Atlantic at 115 kyr BP in most of their experiments. Such an increase of precipitation could contribute to a weakening of the thermohaline circulation in the North Atlantic. Despite the large decrease of the thermohaline circulation between experiment AOVID and experiment AOVID_THC (about 11 Sv difference in maximum Atlantic overturning at 115 kyr BP), the response of our model in terms of ice volume is rather small. Hence, feedbacks related to changes in the thermohaline circulation, as those related to the vegetation, are also not likely to have caused the last glacial inception. However, these feedbacks appear to be a strong amplifier once the inception has started.

9 Summary and conclusions

1. An Earth system model of intermediate complexity, CLIMBER-2, has been used to explore the processes, feedbacks and synergisms that led to the last glacial inception some 120 to 115 kyr BP. The fully coupled atmosphere-ocean-vegetation-inland-ice model successfully simulated the reconstructed ice-volume change both in amplitude and evolution.

2. The last glacial inception appeared in the model as a bifurcation in the physical climate system once a threshold in maximum boreal summer insolation was crossed (Calov et al. part 1). The ice-albedo feedback is the major mechanism, which leads to a rapid expansion of the area covered by inland ice. Feedbacks and synergisms related to vegetation dynamics, ocean dynamics and changes in atmospheric CO_2 concentration serve as important amplifiers, but they are not essential to trigger the last glacial inception in our model. These positive feedbacks considerably contribute to the increase of inland-ice cover.

3. The transition from interglacial to glacial climate appears in our model when pre-industrial atmospheric CO_2 concentration is prescribed instead of changes in atmospheric CO_2 concentration during the last glacial inception according to reconstructions by Barnola et al. (1987). In turn, there was no sign of a glacial

inception in the simulations when the orbital insolation was kept at its present-day value and the atmospheric CO_2 concentration from the palaeo-records (Barnola et al. 1987) was prescribed.

4. The role of mineral dust has been investigated by comparing experiments with fixed present-day dust deposition and with varying dust deposition, respectively. The experiments in which the dust deposition rate was allowed to vary between modern and LGM values - using the modelled ice volume as a weighting factor – were in better agreement regarding geological evidence of inland ice extent than the experiment in which dust deposition was kept constant at present-day values. This indicates that an increase of dust deposition on inland ice may act as regional negative feedback. In this study, only the impact of dust on the albedo of snow, which affects the ablation of the ice sheets, is considered. Radiative effects of airborne dust were ignored in this study.

5. In our simulations, most of the inland ice is formed in North America, while the European ice sheet is relatively small and restricted to Scandinavia. The growth of ice sheets causes a large amount of cooling in the Northern Hemisphere and considerable changes in all components of the climate system. In particular, precipitation is considerably reduced over North America, the Amazon region, North Africa and large parts of Eurasia.

6. The inland-ice cover over Scandinavia has a subtle dependence on changes in the thermohaline circulation of the Atlantic Ocean. Depending on whether the convection site in the North Atlantic is located at a more southern or a more northern position, the climate over Scandinavia is rather moist and warm or, alternatively, dry and cold. In the former case, the ice over Scandinavia builds up in the model to a rather thick ice sheet which is located more in the northern part of this region while in the latter case, the simulated ice sheet is rather thin and located more to the south.

Acknowledgments

The authors wish to thank Ralf Greve for providing us with his polythermal ice-sheet model SICOPOLIS as well as for his assistance. We thank Natalie Mahowald, who sent us her reconstruction of present-day and LGM distributions of dust deposition, and Claire Waelbroeck, who gave us her sea-level record. We further thank two anonymous referees whose thorough reviews improved our earlier manuscript. Alison Schlums helped in editing our manuscript. This work was supported by the Deutsche Forschungsgemeinschaft (research grant CL 178/2-1 and CL 178/2-2) and partly supported by the German Climate Programme DEKLIM (subcontract to BMBF project 01 LD 0041).

References

An Z (2000) The history and variability of the East Asian paleomonsoon climate. Quat Sci Rev 19: 171-187

Bard E, Hamelin B, Fairbanks RG (1990) U-Th ages obtained by mass spectrometry in corals from Barbados: sea level during the past 130,000 years. Nature 346: 456-458

Barnola JM, Raynaud D, Korotkevich YS, Lorius C (1987) Vostok ice core provides 160,000-year record of atmospheric CO_2. Nature 329: 408-414

Berger A (1978) Long-term variations of daily insolation and Quaternary climatic change. J Atmos Sci 35: 2362-2367

Boulton GS, Clark CD (1990) The Laurentide ice sheet through the last glacial cycle: the topology of drift lineations as a key to the dynamic behaviour of former ice sheets. Transactions of the Royal Society of Edinburgh: Earth Sciences 81, 327-347

Brovkin V, Levis S, Loutre MF, Crucifix M, Claussen M, Ganopolski A, Kubatzki C, Petoukhov V (2003) Stability analysis of the climate-vegetation system in the northern high latitudes. Clim Change 57 (1): 119-138

Braconnot P, Joussaume S, Marti O, deNoblet N (1999) Synergistic feedbacks from ocean and vegetation on the African monsoon response to mid-Holocene insolation. Geophys Res Lett 26: 2481-2484.

Calov R, Marsiat I (1998) Simulations of the Northern Hemisphere through the last glacial-interglacial cycle with a vertically integrated and a three-dimensional thermomechanical ice sheet model coupled to a climate model. Ann Glaciol 27: 169-176

Calov R, Ganopolski A, Petoukhov V, Claussen M, Greve R (2005) Transient simulation of the last glacial inception. Part I: Glacial inception as a bifurcation of the climate system. Clim Dyn: revised

Claussen M (2001) Biogeophysical feedbacks and the dynamics of climate. In: Schulze ED, Harrison SP, Heimann M, Holland EA, Lloyd J, Prentice IC, Schimel

D (eds) Global Biogeochemical Cycles in the Climate System. Academic Press, San Diego, pp61-71

Claussen M (ed) (2004) Does land surface matter in climate and weather? In: Kabat P, Claussen M, Dirmeyer P, Gash J, deGuenni, L Meybeck M, Pielke Sr. R, Vörösmarty C, Hutjes R, Lütkemeier S. (eds) Vegetation, Water, Humans and the Climate, Part A. Springer, Heidelberg, in press

Claquin T., Roelandt C, Kohfeld KE, Harrison SP, Tegen I, Prentice IC, Balkanski Y, Bergametti G, Hansson M, Mahowald N, Rodhe H, Schulz M (2003) Radiative forcing of climate by ice-age atmospheric dust. Clim Dyn 20: 193-202

Clark PU, Clague JJ, Curry BB, Dreimanis A, Hicock SR, Miller GH, Berger GW, Eyles N, Lamothe M, Miller BB, Mott RJ, Oldale RN, Stea RR, Szabo JP, Thorleifson LH, Vincent JS (1993) Initiation and development of the Laurentide and Cordilleran ice sheets following the last interglaciation. Quat Sci Rev 12: 79-114

Chappell J, Omura A, Esat T, McCulloch M, Pandolfi J, Ota Y, Pillans B (1996) Reconciliation of late Quaternary sea levels derived from coral terraces at Huon Peninsula with deep sea oxygen isotope records. Earth Planet Sci Lett 141: 227-236

Crowley TJ (1992) North Atlantic Deep Water cools the Southern Hemisphere. Paleoceanography 7: 489-497

Crucifix M, Loutre MF (2002) Transient simulations over the last interglacial period (126-115 kyr BP): feedback and forcing analysis. Clim Dyn 19 (5-6): 417-433 DOI 10.1007/s00382-002-0234-z

Cutler KB, Edwards RL, Taylor FW, Cheng H, Adkins J, Gallup CD, Cutler PM, Burr GS, Bloom AL (2003) Rapid sea-level fall and deep-ocean temperature change since the last interglacial period. Earth Planet Sci Lett 206: 253-271

deNoblet NI, Prentice IC, Joussaume S, Texier D, Botta A, Haxeltine A (1996) Possible role of atmosphere-biosphere interaction in triggering the last glaciation. Geophys Res Lett 23: 3191-3194

Eisenhauer A, Zhu ZR, Collins LB, Wyrwoll K-H, Eichstatter R (1996) The last interglacial sea level change: New evidence from the Abrolhos islands, west Australia. Geologische Rundschau 85: 606-614

Fischer H, Wahlen M, Smith J, Mastroianni D, Deck B et al. (1999) Ice core records of atmospheric CO_2 around the last three glacial terminations. Science 283: 1712-1714

Gallup CD, Cheng H, Taylor FW, Edwards RL (2002) Direct determination of the timing of sea level change during termination II. Science 295: 310-313

Gallée H, van Ypersele JP, Fichefet T, Marsiat I, Tricot C, Berger A (1992) Simulation of the last glacial cycle by a coupled, sectorially averaged climate-ice sheet model. 2. Response to insolation and CO_2 variations. J Geophys Res 97: 15,713-15,740

Gallimore RG, Kutzbach JE (1996) Role of orbital induced changes in tundra area in the onset of glaciation. Nature 381: 503-505

Ganopolski A, Kubatzki C, Claussen M, Brovkin V, Petoukhov V (1998) The influence of vegetation-atmosphere-ocean interactions on climate during the mid-Holocene. Science 280: 1916-1919

Ganopolski A, Rahmstorf S (2001) Rapid changes of glacial climate simulated in a coupled climate model. Nature 409: 153-158

Greve R (1997a) A continuum-mechanical formulation for shallow polythermal ice sheets. Phil Trans R Soc Lond A355: 921-974

Greve R (1997b) Application of a polythermal three-dimensional ice sheet model to the Greenland ice sheet: Response to steady-state and transient climate scenarios. J. Climate 10: 901-918

Hamilton DH (1994) Late Cenozoic glaciation of Alaska. In: Plafker G, Berg HC (eds) The Geology of Alaska: Boulder Colorado, Geological Society of America, The Geology of North America, v. G1, pp 813-844

Imbrie J, Shackleton NJ, Pisias NG, Morley JJ, Prell WL, Martinson DG, Hays JD, McIntyre A, Mix AC (1994) The orbital theory of Pleistocene climate: support from a revised chronology of the marine δ^{18}O record. In: Berger A, Imbrie J, Hays J, Kukla G, Saltzman B (eds) Milankovitch and climate: understanding the response to astronomical forcing. Part I. D. Reidel Publishing Co., Dordrecht, pp 269-305

Ives JD, Andrews JT, Barry RG (1975) Growth and decay of the Laurentide ice sheet and comparison with Fenno-Scandinavia. Naturwissenschaften 62: 118-125

Kageyama M, D'Andrea F, Ramstein G, Valdes PJ, Vautard R (1999) Weather regimes in past climate atmospheric general circulation model simulations. Clim Dyn 15: 773-793

Kageyama M, Charbit S, Ritz C, Khodri M, Ramstein G (2004) Quatifiying ice-sheet feedbacks during the last glacial inception. Geophys Res Lett 31: L24203, DOI: 10.1029/2004GL021339

Kleman J, Hättestrand C, Borgström I, Stroeven A (1997) Fennoscandian palaeoglaciology reconstructed using a glacial geological inversion model. J Glaciol 43: 283-299

Khodri M, Leclainche Y, Ramstein G, Braconnot P, Marti O, Cortijo E (2001) Simulating the amplification of orbital forcing by ocean feedbacks in the last glaciation. Nature 410: 570-574

Khodri M, Ramstein G, Paillard D, Duplessy JC, Kageyama M, Ganopolski A (2003) Modelling the climate evolution from the last interglacial to the start of the last glaciation: The role of Arctic Ocean freshwater budget. Geophys Res Lett 30 (12): 1606, DOI: 10.1029/2003GL017108

Loutre MF, Berger A (2000) No glacial-interglacial cycle in the ice volume simulated under a constant astronomical forcing and a variable CO_2. Geophys Res Lett 27(6): 783-786

Mahowald N, Kohfeld KE, Hansson M, Balkanski Y, Harrison SP, Prentice IC, Schulz M, Rodhe H (1999) Dust sources and deposition during the last glacial maximum and current climate: A comparison of model results with paleodata from ice cores and marine sediments. J Geophys Res 104: 15,895-15,916

Marsiat I (1994) Simulation of the Northern Hemisphere continental ice sheets over the last Glacial-Interglacial Cycle: experiments with a latitude-longitude vertically integrated ice-sheet model coupled to zonally averaged climate model. Paleoclimates 1: 59-98

Mangerud J (1991) The Scandinavian ice sheet through the last interglacial/glacial cycle. In: Frenzel B (ed) Klimageschichtliche Probleme der letzten 130,000 Jahre, G. Fischer, Stuttgart, New York, pp. 307-330

Meissner KJ, Weaver AJ, Matthews HD, Cox PM (2003) The role of land surface dynamics in glacial inception: a study with the UVic Earth System Model. Clim Dyn 21: 515-537 DOI 10.1007/s00382-003-0352-2

Peltier WR, Marshall S (1995) Coupled energy-balance/ice-sheet model simulations of the glacial cycle: A possible connection between terminations and terrigenous dust. J Geophys Res 100: 14,267-14,289

Petoukhov V, Ganopolski A, Brovkin V, Claussen M, Eliseev A, Kubatzki C, Rahmstorf S (2000) CLIMBER-2: a climate system model of intermediate complexity. Part I: model description and performance for present climate. Clim Dyn 16: 1-7

Peixoto JP, Oort AH (1992) Physics of climate, 1st edn. American Institute of Physics, New York, pp 298-299

Petit JR, Jouzel J, Raynaud D, Barkov NI, Barnola JM, Basile I, Bender M, Chappellaz J, Davis M, Delaygue G, Delmotte M, Kotlyakov VM, Legrand M, Lipenkov VY, Lorius C, Pepin L, Ritz C, Saltzman E, Stievenard M (1999) Climate and atmospheric history of the past 420,000 years from the Vostok ice core, Antarctica. Nature 399: 429-436

Pollard D, Thompson SL (1997) Driving a high-resolution dynamic ice-sheet model with GCM climate: ice-sheet initiation at 116 000 BP. Ann Glaciol 25: 296-304

Porter SC (2001) Chinese loess record of monsoon climate during the last glacial-interglacial cycle. Earth Science Reviews 54: 115-128

Prentice IC, Cramer W, Harrison SP, Leemans R, Monserud RA, Solomon AM (1992) A Global Biome Model Based on Plant Physiology and Dominance, Soil Properties and Climate. J Biogeogr 19: 35-57

Tarasov L, Peltier WR (1997) Terminating the 100 kyr ice age cycle. J Geophys Res 102: 21,665-21,693

Vettoretti G, Peltier WR (2004) Sensitivity of glacial inception to orbital and greenhouse gas climate forcing. Quat Sci Rev 23: 499-519

Verbitsky and Oglesby (1992) The effect of atmospheric carbon dioxide concentration on continental glaciation of the northern Hemisphere. J Geophys Res 97 (D5): 5895-5909

Waelbroeck C, Labeyrie L, Michel E, Duplessy JC, McManus JF Lambeck K, Balbon E, Labracherie M (2002) Sea-level and deep water temperature changes derived from benthic formaminifera isotopic records. Quat Sci Rev 21: 295-305

Wang Z, Mysak LA (2002) Simulation of the last glacial inception and rapid ice sheet growth in the McGill Paleoclimate Model. Geophys Res Lett 29: 2102, DOI: 10.1029/2002GL015120

Warren SG, Wiscombe WJ (1980) A model for the spectral albedo of snow. II: Snow containing atmospheric aerosol. J Atmos Sci, 37:2734-2745

Zhu ZR, Wyrwoll K-H, Collins LB, Chen JH, Wasserburg GJ, Eisenhauer A (1993) High precision U-series dating of Last Interglacial events by mass spectrometry: Houtman Abrolhos Island, western Australia. Earth Planet Sci Lett 118: 281-293

Figure Captions

Figure 1. Mineral dust on the Northern Hemisphere after Mahowald et al. (1999): (**a**) Dust-deposition rate at present day in g m^{-2} yr^{-1}, (**b**) Ratio of LGM to present-day dust-deposition rate.

Figure 2. Relative sea level in experiments AOVI and AOVID (see table 1 for the notation) compared with proxy data**.** The continuous sea-level curves are after Imbrie et al. (1984) (labelled as **SPECMAP**) and Waelbroeck et al. (2002) (labelled as **C.W. et al. 2002**). The full circles correspond to coral data from various sources (Bard, et al., 1990; Chappell et al., 1996; Eisenhauer et al., 1996, Cutler et al., 2003; Gallup et al., 2002; Zhu et al. 1993). The symbols on the top of the figure indicate marine isotope stages.

Figure 3. Spatial extent of ice area on the Northern Hemisphere: (**a**, **c**, **e)** simulations with constant present-day dust (AOVI), (**b**, **d**, **f)** simulations with time-dependent dust distribution (AOVID). Times are at (**a**, **b**) 115 kyr BP, (**c**, **d**) 110 kyr BP and (**e**, **f**) 105 kyr BP.

Figure 4. Surface elevation of the inland ice in northern North America in experiment AOVID: (**a)** 118 kyr BP, (**b)** 117 kyr BP and (**c)** 110 kyr BP.

Figure 5. Time series: (**a)** ice volume and (**b)** ice area of the North American inland ice and the same for (**c** and **d**) the European inland ice for different scenarios (set inset). Note that the scale of the ordinates differs by one order of magnitude for North America and Europe. Here, the "European inland ice" includes the ice sheets in Scandinavia, Svalbard and Iceland, but excludes the Greenland ice sheet and possible ice sheets in north-eastern Eurasia. Ice volume is in 10^6 km^3 and ice area in 10^6 km^2.

Figure 6. Anomalies (changes with respect to present-day values): (**a**, **c**) temperature and (**b**, **d**) precipitation in boreal summer for experiment AOVID. Times are at (**a, b**) 118 kyr BP and (**c**, **d**) 115 kyr BP. Temperature is in °C and precipitation in $mm\,day^{-1}$.

Figure 7. Time series of total inland-ice cover without Greenland: (**a)** experiments AOVID, AOID, AVID and AID, (**b)** experiments AOVID, AOVID_280 and AOVID_PDI. See table 1 for the notation of the experiments. The area is given in 10^6 km^2.

Figure 8. Simulated forest fractions in percentage: (**a)** the present-day steady state; and in experiment AOVID at (**b)** 125 kyr BP, (**c)** 115 kyr BP, and (**d)** 105 kyr BP.

Figure 9. Annual temperature anomalies between experiments AOVID and AOID: (**a)** at 125 kyr BP, (**b)** at 118 kyr BP, and (**c)** at 115 kyr BP.

Figure 10. Anomalies between experiments AOVID_THC and AOVID at 110 kyr BP: (**a)** the annual precipitation in $mm\,day^{-1}$ and (**b)** the summer temperature in °C.

Figure 11. Surface elevation in km at 110 kyr BP: (**a)** experiment AOVID and (**b)** experiment AOVID_THC. The solid line indicates the coast and the dashed line shows the ice margins.

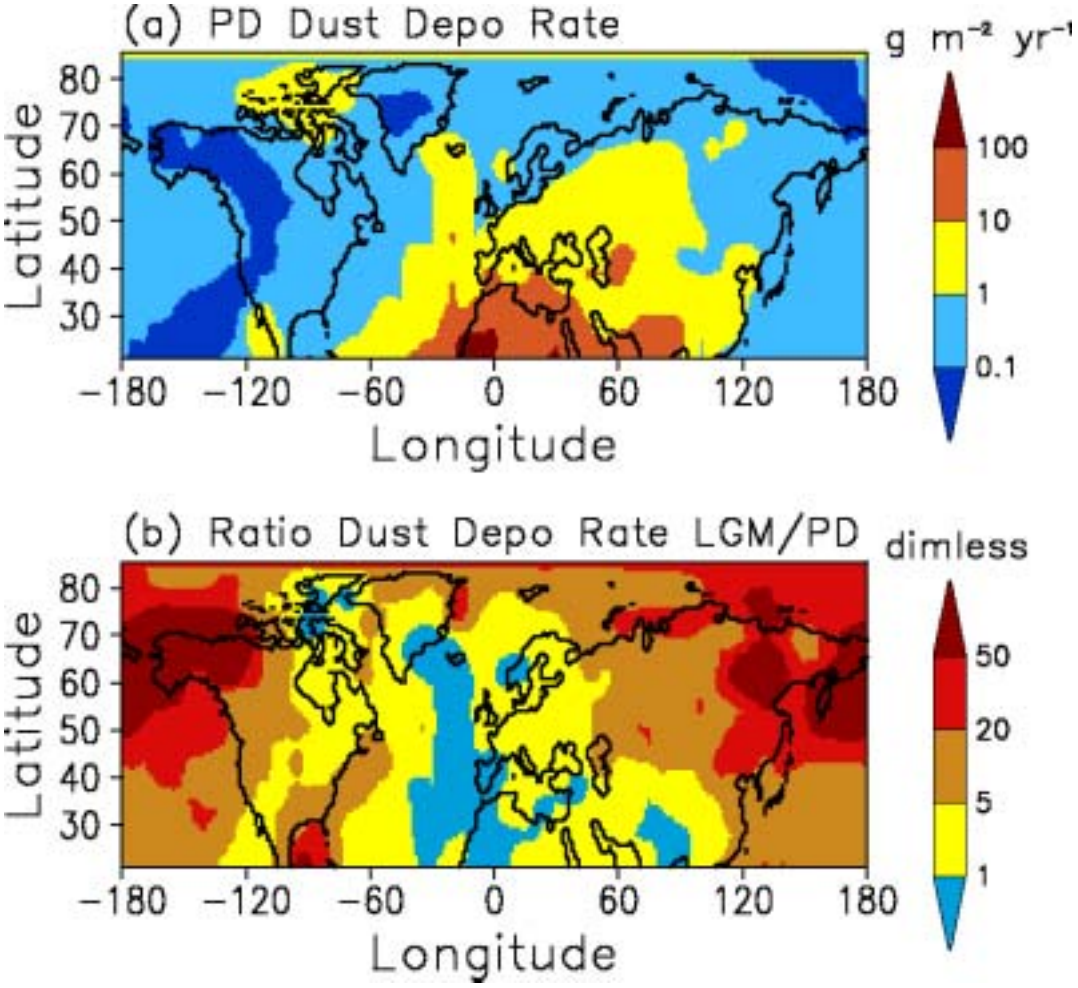
(a) PD Dust Depo Rate
g m⁻² yr⁻¹
100
10
1
0.1
Latitude
80
70
60
50
40
30
−180 −120 −60 0 60 120 180
Longitude
(b) Ratio Dust Depo Rate LGM/PD
dimless
50
20
5
1
Latitude
80
70
60
50
40
30
−180 −120 −60 0 60 120 180
Longitude

Figure 1

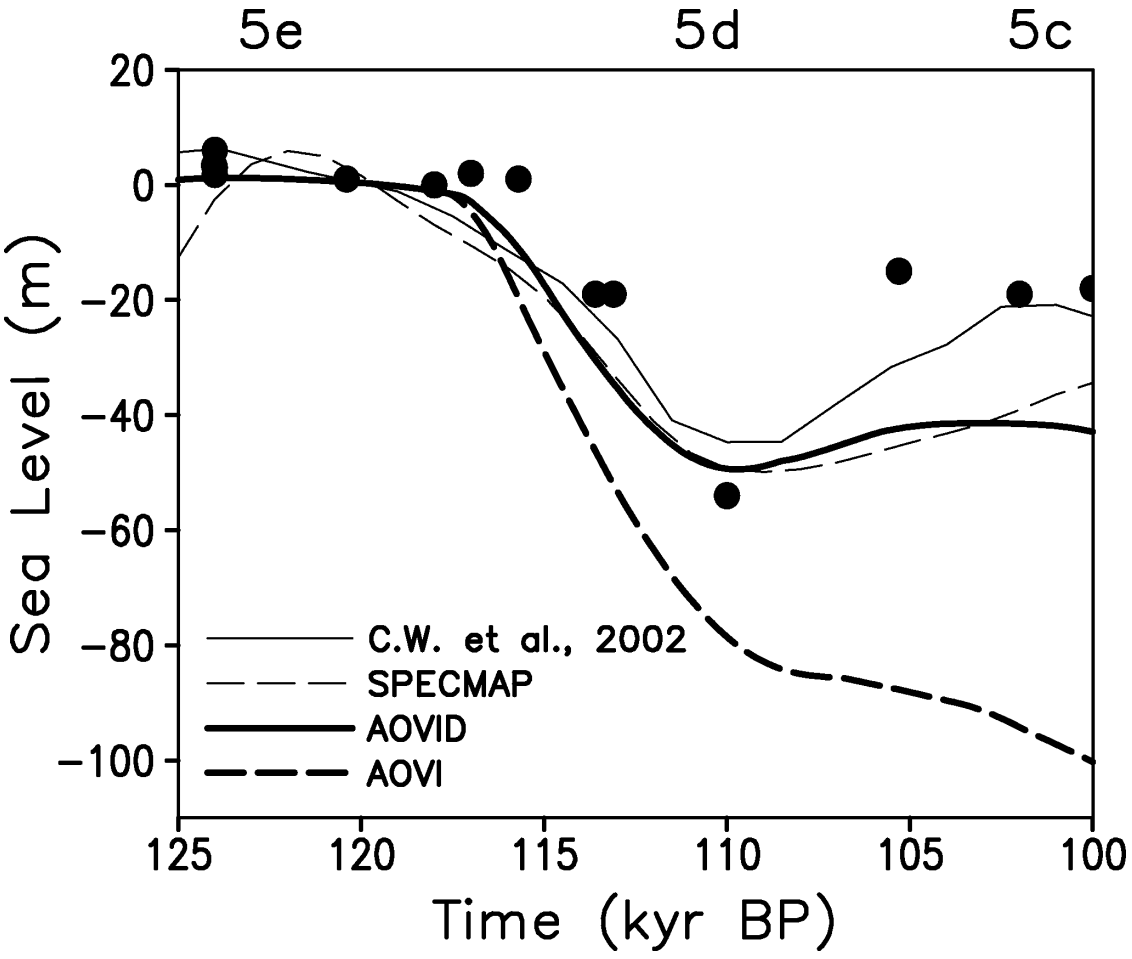
5e
5d
5c
20
0
−20
−40
−60
−80
−100
Sea Level (m)
C.W. et al., 2002
SPECMAP
AOVID
AOVI
125
120
115
110
105
100
Time (kyr BP)

Figure 2

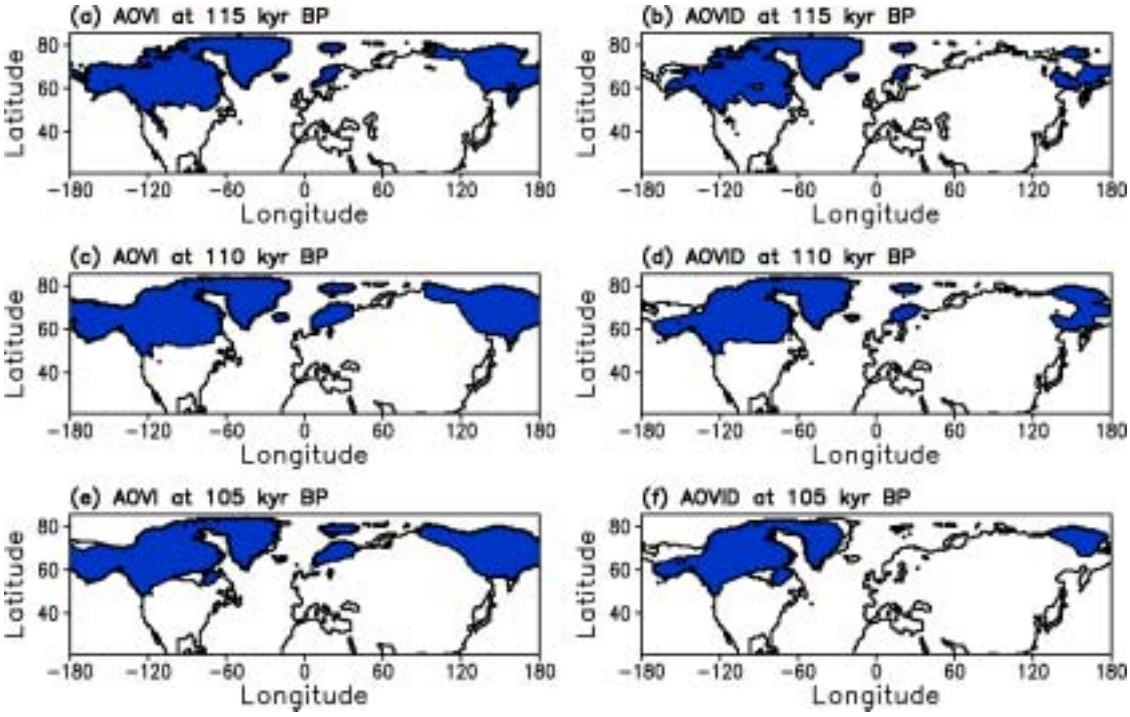
(a) AOVI at 115 kyr BP
(b) AOVID at 115 kyr BP
(c) AOVI at 110 kyr BP
(d) AOVID at 110 kyr BP
(e) AOVI at 105 kyr BP
(f) AOVID at 105 kyr BP
Latitude
Longitude
80
60
40
−180
−120
−60
0
60
120
180

Figure 3

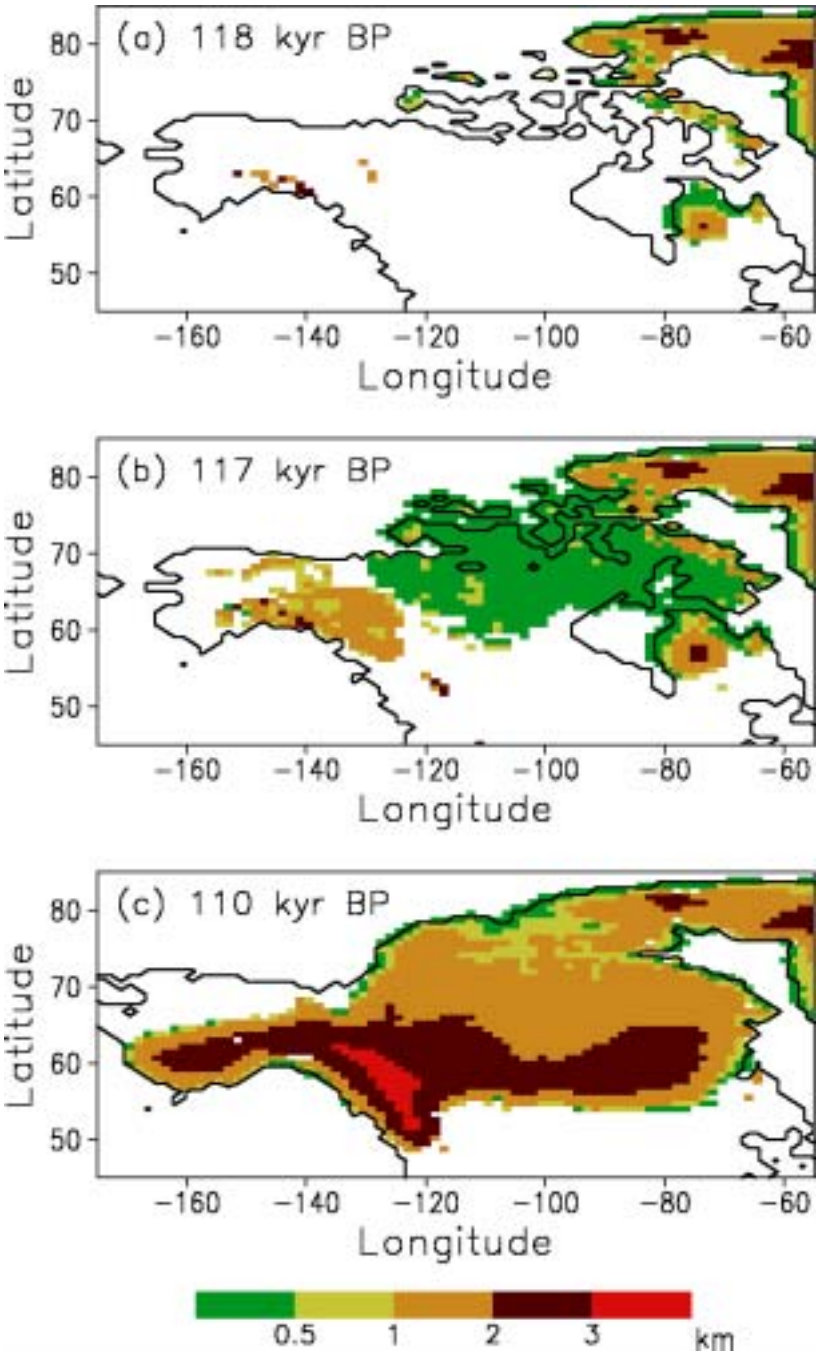
(a) 118 kyr BP
(b) 117 kyr BP
(c) 110 kyr BP
Latitude
Longitude
80
70
60
50
−160
−140
−120
−100
−80
−60
0.5
1
2
3
km

Figure 4

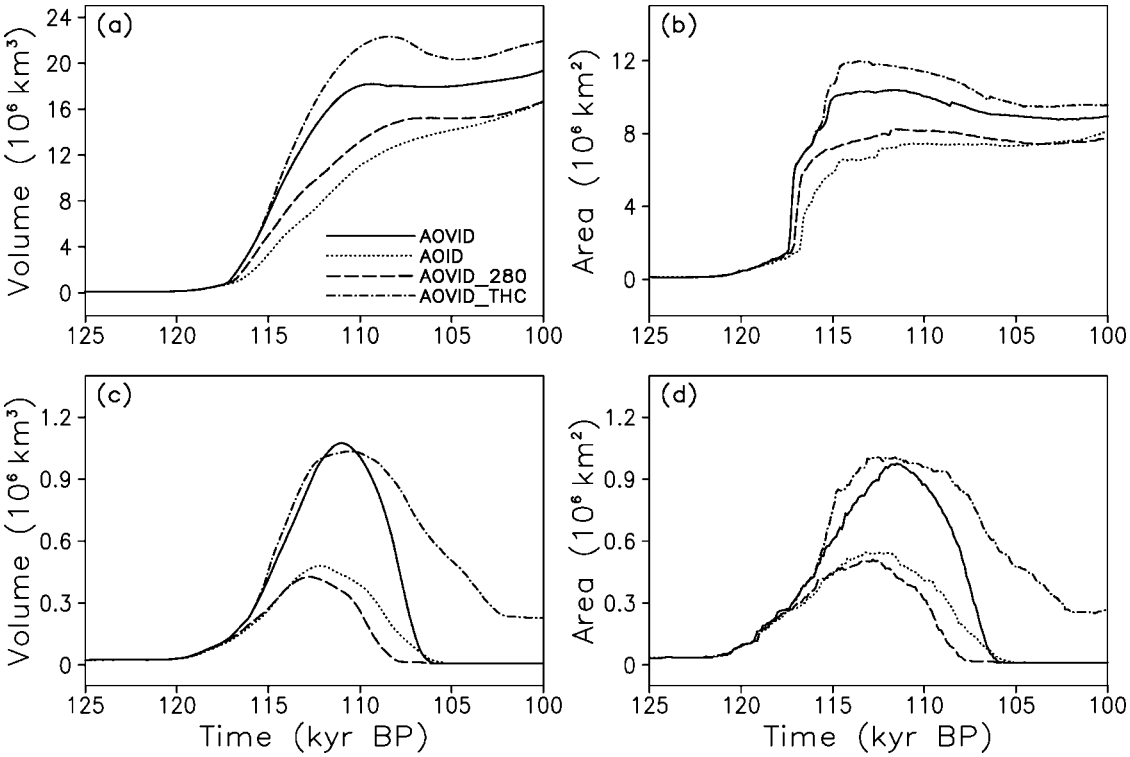
(a)
(b)
(c)
(d)
Volume (10⁶ km³)
Area (10⁶ km²)
Time (kyr BP)
AOVID
AOID
AOVID_280
AOVID_THC

Figure 5

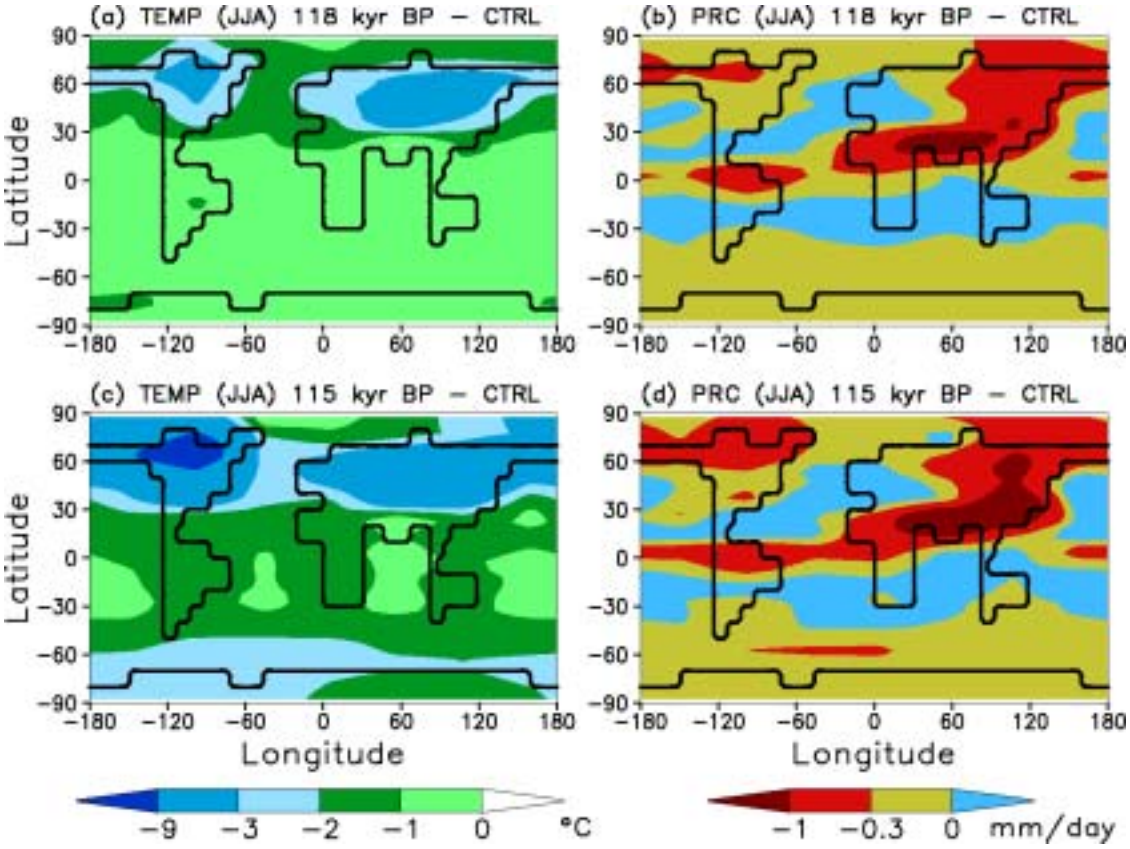
(a) TEMP (JJA) 118 kyr BP – CTRL
(b) PRC (JJA) 118 kyr BP – CTRL
(c) TEMP (JJA) 115 kyr BP – CTRL
(d) PRC (JJA) 115 kyr BP – CTRL
Latitude
Longitude
90
60
30
0
−30
−60
−90
−180
−120
−60
0
60
120
180
−9
−3
−2
−1
0
°C
−1
−0.3
0
mm/day

Figure 6

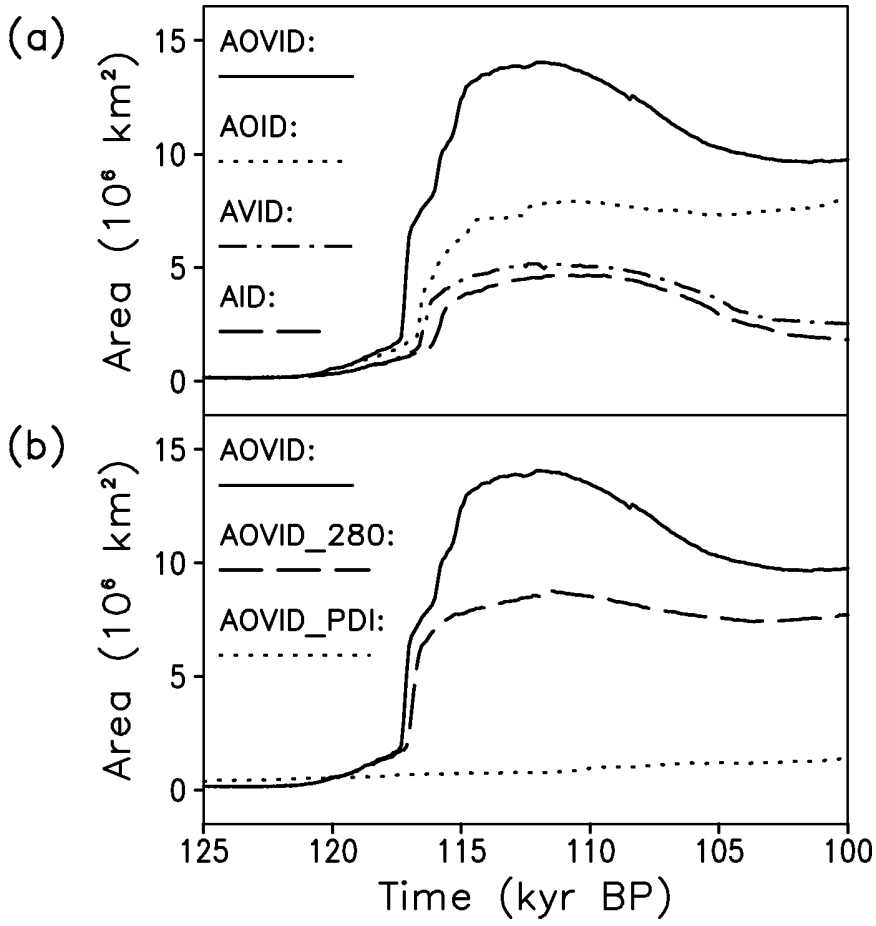
(a)
AOVID:
AOID:
AVID:
AID:
Area (10^6 km^2)
15
10
5
0
(b)
AOVID:
AOVID_280:
AOVID_PDI:
Area (10^6 km^2)
15
10
5
0
125
120
115
110
105
100
Time (kyr BP)

Figure 7

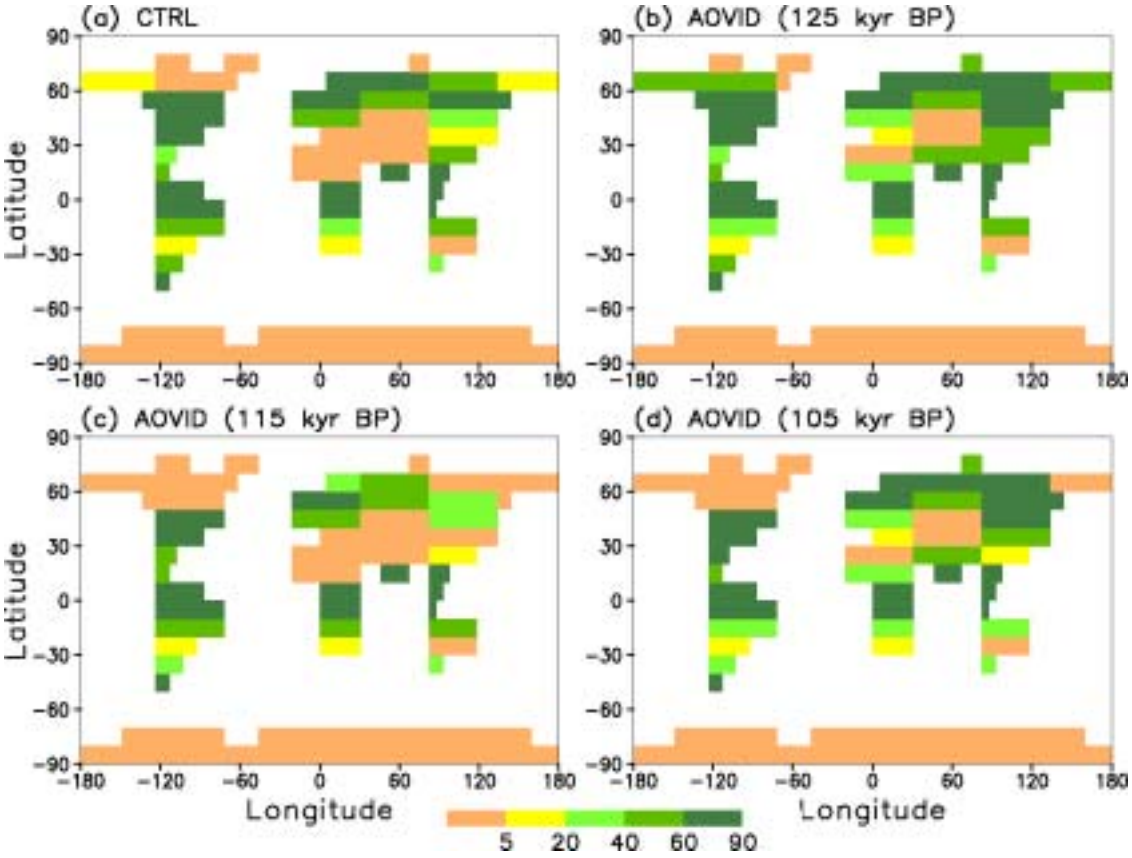
(a) CTRL
(b) AOVID (125 kyr BP)
(c) AOVID (115 kyr BP)
(d) AOVID (105 kyr BP)
Latitude
Longitude
90
60
30
0
−30
−60
−90
−180
−120
−60
0
60
120
180
5
20
40
60
90

Figure 8

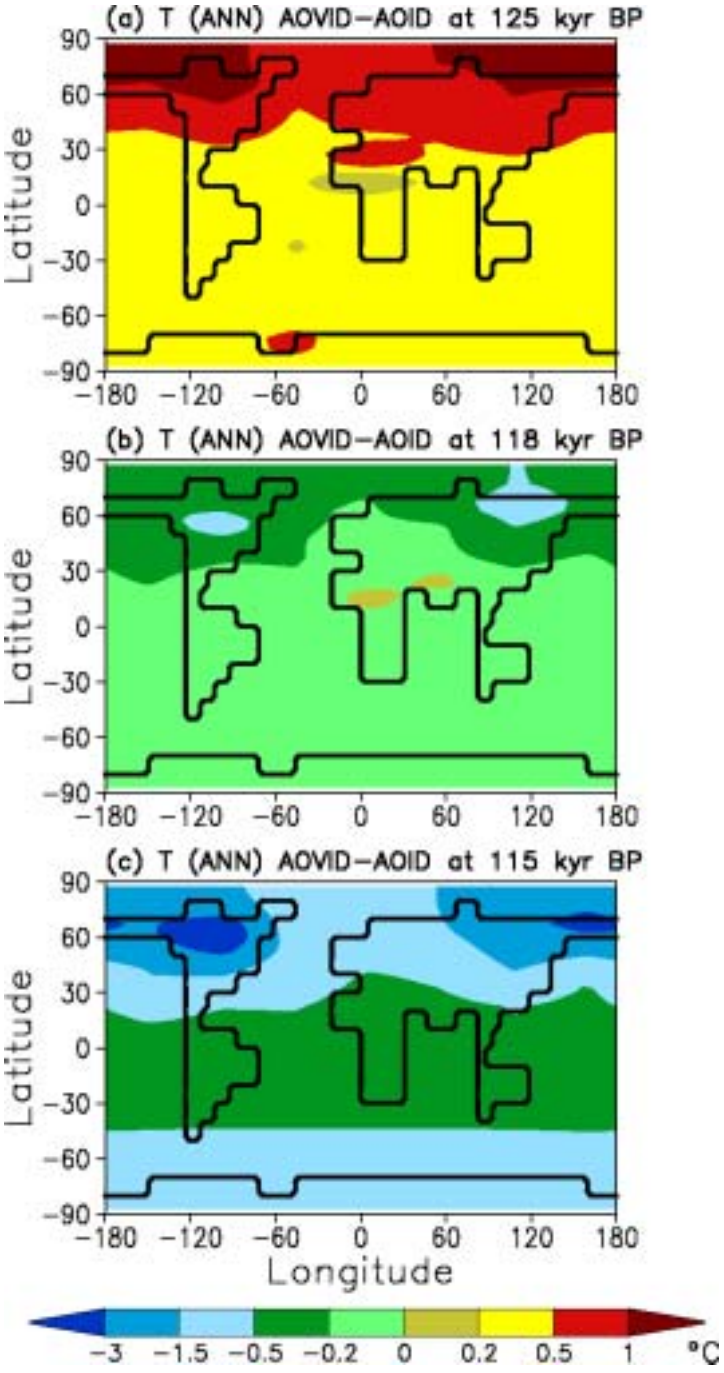
(a) T (ANN) AOVID−AOID at 125 kyr BP
(b) T (ANN) AOVID−AOID at 118 kyr BP
(c) T (ANN) AOVID−AOID at 115 kyr BP
Latitude
Longitude
90
60
30
0
−30
−60
−90
−180 −120 −60 0 60 120 180
−3 −1.5 −0.5 −0.2 0 0.2 0.5 1 °C

Figure 9

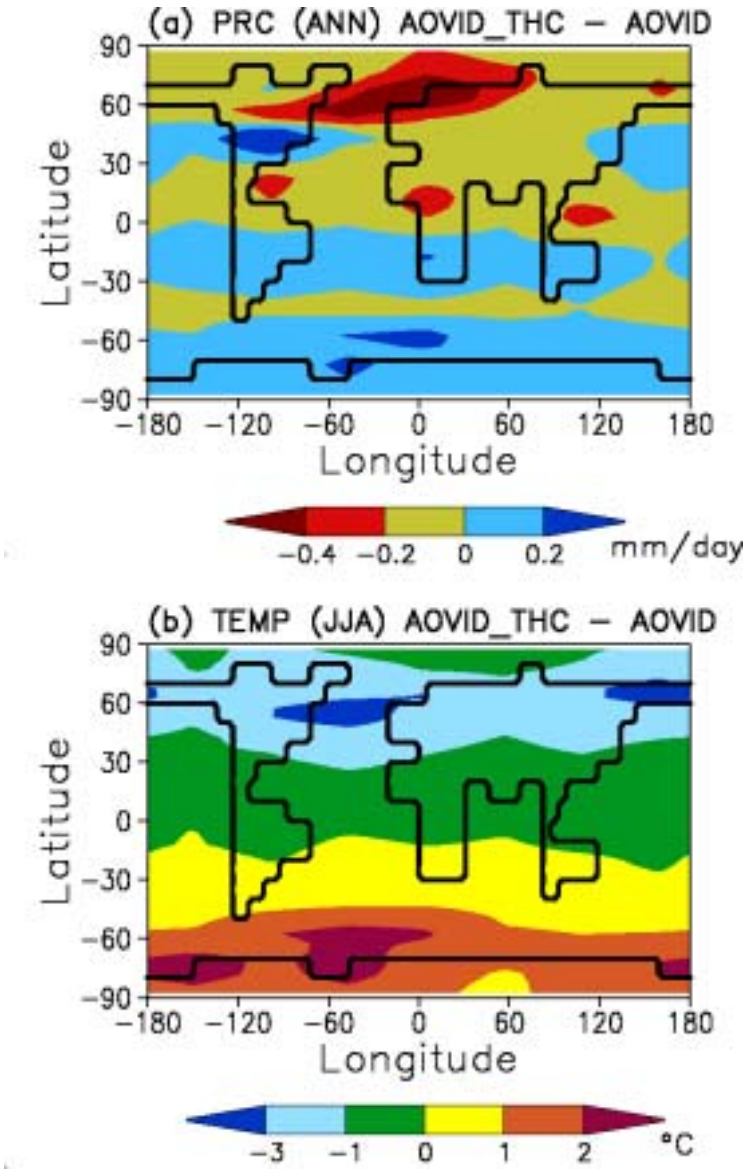
(a) PRC (ANN) AOVID_THC – AOVID
Latitude
90
60
30
0
-30
-60
-90
-180 -120 -60 0 60 120 180
Longitude
-0.4 -0.2 0 0.2
mm/day
(b) TEMP (JJA) AOVID_THC – AOVID
Latitude
90
60
30
0
-30
-60
-90
-180 -120 -60 0 60 120 180
Longitude
-3 -1 0 1 2
°C

Figure 10

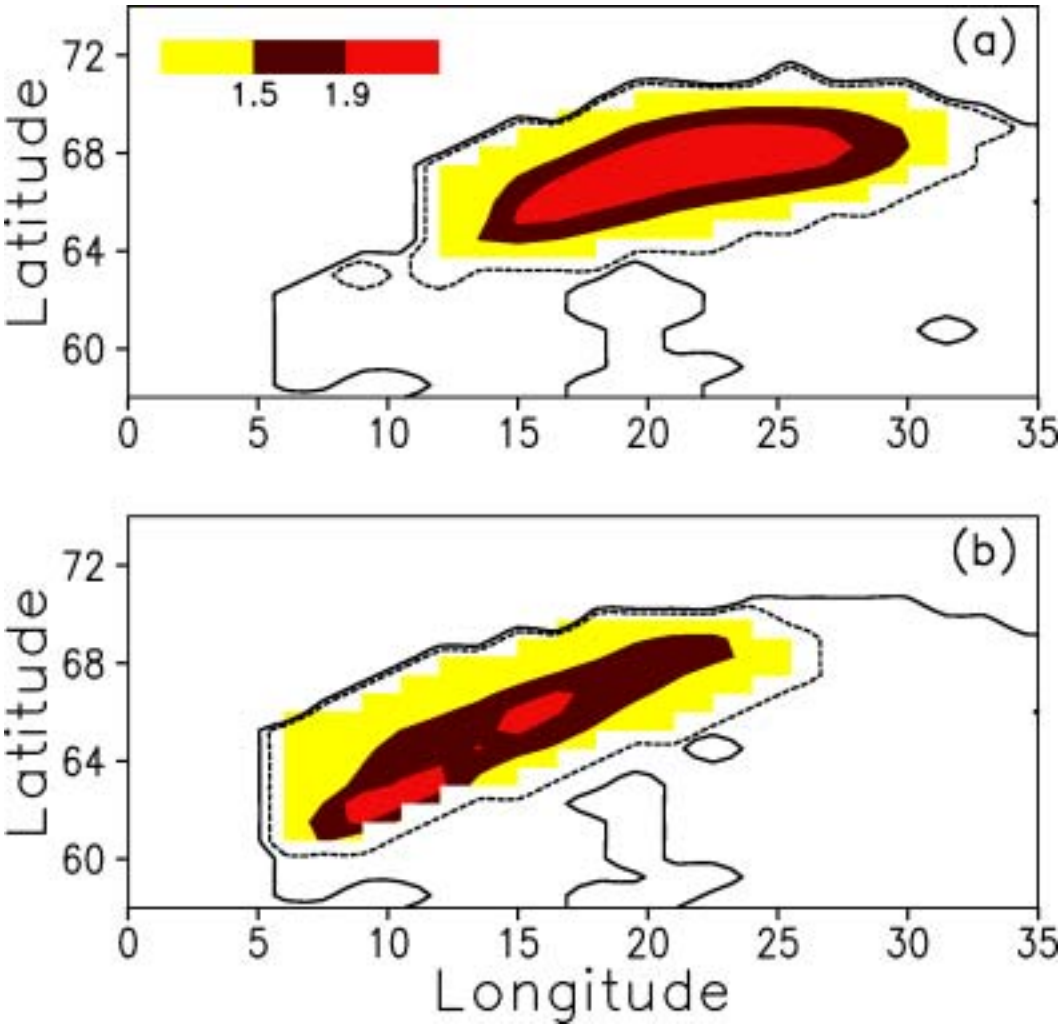
(a)
1.5
1.9
Latitude
72
68
64
60
0
5
10
15
20
25
30
35
(b)
Latitude
72
68
64
60
0
5
10
15
20
25
30
35
Longitude

Figure 11